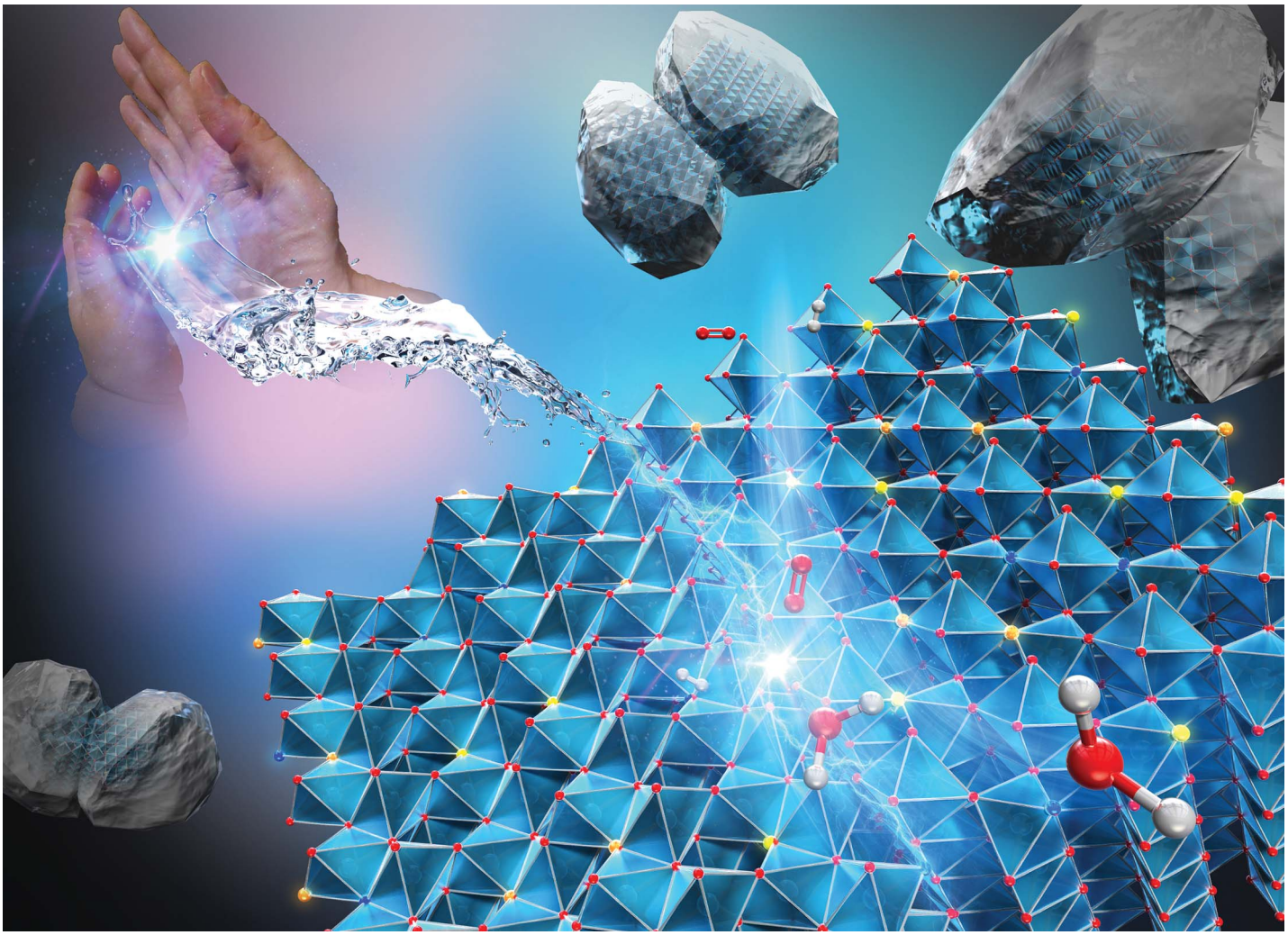

Showcasing the collaborative research on non-platinum fuel cell catalysts by Professor Chisaka from Hirosaki University in Japan and Professor Daiguji group from the University of Tokyo in Japan.

S-doped TiN supported N, P, S-tridoped TiO_2 with hetero-phase junctions for fuel cell startup/shutdown durability

A new strategy for the dramatic enhancement of both oxygen reduction reaction (ORR) activity and durability above 1.0 V, of TiO_2 catalyst is revealed. By introducing hetero-phase junctions from two different TiO_2 phases and a new anionic sulfur dopant, S-doped TiN supported N, P, S-tridoped TiO_2 catalyst exhibits higher ORR activity and durability than reported for other oxide/oxynitride catalysts. In particular, the durability during startup/shutdown cycles ranks the highest among the platinum-group-metal free catalysts, which opens the door to significantly reducing the production and operating costs of fuel cell vehicles.

As featured in:

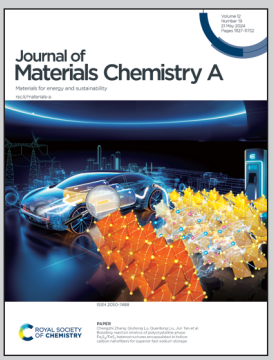

See Mitsuharu Chisaka *et al.*, *J. Mater. Chem. A,* 2024, **12**, 11277.

ROYAL SOCIETY OF CHEMISTRY

rsc.li/materials-a

Registered charity number: 207890

Journal of Materials Chemistry A

ROYAL SOCIETY OF CHEMISTRY

PAPER

View Article Online
View Journal | View Issue

Cite this: J. Mater. Chem. A, 2024, 12, 11277

S-doped TiN supported N, P, S-tridoped TiO_2 with hetero-phase junctions for fuel cell startup/shutdown durability†

Mitsuharu Chisaka, *[a] Jubair A. Shamim,[b] Wei-Lun Hsu [b] and Hirofumi Daiguji [b]

Received 3rd March 2024
Accepted 17th April 2024

DOI: 10.1039/d4ta01475h

rsc.li/materials-a

TiO_2 layers codoped with N and P formed on S-doped TiN are recently developed platinum-group metal (PGM)-free catalysts (N, P-TiO_2/S-TiN) for the oxygen reduction reaction (ORR) in acidic media. Conventional Pt-based catalysts lack durability as the necessary carbon supports are oxidized at high potentials (>1.0 V) during startup and shutdown. N, P-TiO_2/S-TiN catalysts do not require carbon supports and are expected to tolerate oxidation at high potentials. However, N, P-TiO_2/S-TiN loses ORR activity during startup or shutdown at potentials >1.0 V due to removal of N- and P-atoms. We therefore report a new pathway to enhance durability and ORR activity of N, P-TiO_2/S-TiN. By annealing N, P-TiO_2/S-TiN with NH_4F under N_2, ORR active anatase/rutile TiO_2 hetero-phase junctions are produced in bulk with remaining TiN supports, and the surface O-atoms in the TiO_2 lattice are substituted by S^{2-}. S-doped TiN-supported N, P, S-tridoped TiO_2 exhibits the highest ORR activity among reported oxide/oxynitride catalysts, although the ORR activity of the N, P, S-TiO_2/S-TiN catalyst remains lower than that of state-of-the-art carbon-based catalysts. The N, P, S-TiO_2/S-TiN catalyst exhibits superior durability among PGM-free catalysts as the anionic dopants are not removed after 5000 potential cycles (1.0–1.5 V), leading to a 0.02 V reduction in half-wave potential.

1. Introduction

The global transport sector currently accounts for one-quarter of energy consumption overall, and is responsible for approximately 40% of carbon emissions from end-use sectors.[1] In 2021, road vehicles emitted 5.9 gigatons of CO_2, representing three-quarters of all CO_2 emissions from the transport sector.[1] By the end of 2020, the total number of vehicles globally reached 1.5 billion, including 1.1 billion passenger vehicles and 0.4 billion buses or trucks.[2] Government regulations to limit emissions from passenger vehicles are becoming increasingly stringent, and some countries and regions plan to phase out passenger vehicles powered by the conventional internal combustion engine (ICE) between 2025 and 2040.[3]

Polymer electrolyte fuel cells (PEFCs) have emerged as a promising alternative to ICEs in light-duty passenger vehicles for journeys over 300 miles,[4] as well as in mid- to heavy-duty vehicles.[5] Although PEFC-powered passenger vehicles have been available since 2014, they still constitute a small percentage of the current market share. At present, carbon-supported platinum (Pt/C) and platinum-cobalt (PtCo/C) catalysts are the most common means to catalyze the hydrogen oxidation reaction (HOR) at the anode and the oxygen reduction reaction (ORR) at the cathode of PEFC catalyst layers, respectively.[5,6] Cathode platinum loading is typically four-times higher than that of the corresponding anode due to the slower kinetics of ORR compared with HOR.[7] The high platinum loading requirement is assumed to be the greatest cost barrier to the widespread adoption of fuel cell vehicles (FCVs).[8] Therefore, efforts have been made over the last two decades to reduce the amount of platinum required in PEFCs by an order of magnitude, to ~20 g per 128 kW class passenger vehicle.[4,6] However, a further reduction to ~6 g per vehicle is necessary to make PEFC-powered passenger vehicles affordable and allow them to become widespread.[7]

In addition to the high costs, carbon-supported platinum-based catalysts currently lack stability, with the instability of platinum/platinum-alloy catalysts and corrosion of carbon supports being identified as major challenges in improving the durability of PEFC stacks.[8] In an ideal PEFC, the anode and cathode reactions would be described as follows (eqn (1) and (2)):

$$\text{HOR at anodes: } H_2 \rightarrow 2H^+ + 2e^- \quad (1)$$

[a]Department of Sustainable Energy, Hirosaki University, 3 Bunkyo-cho, Hirosaki, Aomori 036-8561, Japan. E-mail: chisaka@hirosaki-u.ac.jp

[b]Department of Mechanical Engineering, The University of Tokyo, 7-3-1, Hongo, Bunkyo-ku, Tokyo 113-8656, Japan

† Electronic supplementary information (ESI) available: Experimental details, XRD patterns, XP spectra, RDE voltammograms and TEM images. See DOI: https://doi.org/10.1039/d4ta01475h

$$\text{ORR at cathodes: } O_2 + 4H^+ + 4e^- \rightarrow 2H_2O \quad (2)$$

During the startup or shutdown of PEFCs, the anode is contaminated with oxygen molecules originating either from the cathode or the air. Later, the contaminating oxygen molecules are reduced to water as the anode Pt/C catalyzes the ORR (eqn (2)), giving rise to a counter cathode potential of up to ~1.5 V *via* a reverse current decay mechanism.[9] Carbon blacks in a PtCo/C cathode are oxidized *via* eqn (3) at such high potentials.

$$C + 2H_2O \rightarrow CO_2 + 4H^+ + 4e^- \quad (3)$$

The PtCo nanoparticles on the carbon supports can no longer be used once the carbon supports are corroded. To avoid this issue, carbon supports are usually protected by system-level measures, such as reducing the cathode air flow rate during shutdown to minimize O_2 diffusion to the anode and injecting a small amount of H_2 to the anode during FCV off-time to react with O_2 contaminants.[10] However, as these measures further increase the cost of FCVs, considerable efforts have been made over the last two decades to develop carbon-free materials as supports for platinum or platinum alloys.[11–14]

The high loading of expensive and scarce platinum catalysts and the low durability of carbon supports are the major motivations to seek cathode catalysts that do not use platinum-group metals (PGMs) or carbon supports. Researchers in the PGM-free catalyst community have developed so-called M/N/C catalysts, which are graphitic carbons with abundant defects doped with N and one or two metals (M); typically Fe,[15–20] Co,[21] or Mn.[22] The highest activity reported to date has been seen with Fe/N/C catalysts, although durability remains an issue, as explored in the literature. The formation of carbon dioxides by the oxidation of carbon species has been experimentally verified, even at potentials below 1.0 V,[16,18,21] and is regarded as one of the pivotal causes of the degradation of M/N/C catalysts. To minimize carbon oxidation, a recent standardized protocol for evaluating the activity of M/N/C catalysts has limited the upper potential to 0.925 V, which is lower than that for automotive carbon-supported platinum-cobalt catalysts (0.95 or 1.0 V).[20] The equilibrium potential in eqn (3) with respect to a standard hydrogen electrode is 0.207 V, and the reaction rate in eqn (3) is accelerated at high potentials. Thus, even when M/N/C catalysts are used, the system-level measures for protecting the carbon blacks of PtCo/C catalysts, as mentioned above, are also necessary.

Oxide/oxynitride-type catalysts containing group IV or V metals have been less well studied in the field of PGM-free catalysts owing to their low conductivity when compared with M/N/C catalysts; a property which also acts as a barrier for activity evaluation.[23] Zirconium oxynitride (ZrO_xN_y) nanoparticles have shown the best activity in this type of catalyst after being supported on conductive multiwall carbon nanotubes (MWCNTs). However, as MWCNTs were found not to be sufficiently conductive, carbon blacks were added to ZrO_xN_y-MWCNT catalysts to enhance the conductivity in the catalyst layer.[24] Nevertheless, the resulting durability was still insufficient, even below 1.0 V.[24]

We have thus shifted our attention toward nitrogen-doped titanium dioxide (TiO_2) layer catalysts formed on conductive titanium nitride (TiN) particles without employing any carbon supports.[25–29] Various control experiments confirmed that both the activity and conductivity of the catalyst originated from TiN, not from the carbon residues of the urea precursor.[25,26] Recently, P- and N- atoms were codoped into the surface TiO_2 layer on TiN.[27,28] This led to enhanced activity and durability due to the augmented surface phosphorous doping level, and the catalyst exhibited no degradation after repeated load cycling tests at potentials of 0.6 and 1.0 V.[28] Since the catalyst was free from carbon supports, there was no corrosion of carbon support as shown in eqn (3); however, after startup/shutdown tests in which the potential was cycled between 1.0 and 1.5 V, the activity deteriorated significantly due to removal of surface P- and N-atoms.[27,28] In particular, a large number of N-atoms substituting for O-atoms in the TiO_2 lattice were removed after 5000 cycles.[28] Thus, high-cost measures to maintain the potential below 1.0 V are still necessary for the utilization of P- and N-codoped TiO_2 catalysts (hereafter denoted as N, P-TiO_2/S-TiN as bulk TiN contains sulfur species from the precursor, which is described later), despite the absence of carbon supports.

Here, we report a new strategy for the dramatic enhancement of both ORR activity and startup/shutdown durability above 1.0 V by introducing (1) hetero-phase junctions from two different TiO_2 phases (anatase and rutile in bulk) and (2) a new dopant (S-atoms which substituted for O-atoms in the surface TiO_2). This approach resulted in higher ORR activity and durability than reported for other oxide/oxynitride catalysts. In particular, durability during startup/shutdown cycles ranks the highest among the PGM-free catalysts, which opens the door to significantly reducing the production and operating costs of FCVs.

2. Experimental methods

2.1. Catalyst synthesis

The N, P-TiO_2/S-TiN catalysts were synthesized using a recently reported solution phase combustion route,[28] and the details of catalyst synthesis and characterization methods are described in S1; ESI.† Briefly, powders of titanium oxysulfate, urea, and hypophosphorous acid solution were mixed in 1.0 mol dm^{-3} hydrochloric acid solution at room temperature. The mass ratio of urea to titanium oxysulfate-derived TiO_2 was set at 100. The atomic ratio of phosphorous to titanium was set at 0.2, which is the optimized value for the activity.[28] The dispersion was then heated with continuous mixing, followed by drying. The dried powders were pyrolyzed at 1173 K for 2 h under N_2 gas. Then the obtained catalysts and ammonium fluoride (NH_4F) powders were ground in an agate mortar and annealed under N_2 gas at various temperatures and for different durations to yield TiO_2 catalysts doped with N-, P- and S-atoms; hereafter denoted as N, P, S-TiO_2/S-TiN.

2.2. Characterization

The bulk and outermost surface structures of catalysts were investigated by analyzing X-ray diffraction (XRD) patterns and ultraviolet (UV)-Raman spectra, respectively. The chemical states of the catalysts were determined by X-ray photoelectron spectroscopy (XPS). The peak shifts due to surface charge were corrected using the binding energy of C 1s (284.8 eV), originating from the hydrocarbon contaminants in the spectrometer or air. The morphology of the N, P, S-TiO_2/S-TiN catalysts was investigated by transmission electron microscopy (TEM) images. Elemental compositions were evaluated using energy dispersive X-ray spectroscopy (EDS).

2.3. ORR activity, selectivity, and durability measurements

Rotating disk electrode (RDE) and rotating ring disk electrode (RRDE) voltammograms were obtained to evaluate the ORR activity and selectivity, respectively, of the catalysts. The mass fraction of Nafion in the catalyst layer was set at 0.05 and the catalyst loading was set at 0.86 mg cm^{-2} unless otherwise noted. A conventional three-electrode cell was used for the room-temperature electrochemical measurements performed in 0.1 mol dm^{-3} H_2SO_4. After sequentially bubbling O_2 and N_2 for 1800 s, RDE and RRDE voltammograms were recorded by applying a disk potential (E) of 0.05–1.2 V *versus* the reversible hydrogen electrode (RHE) at a scan rate of 5 mV s^{-1} and a rotation speed of 1500 rpm. The ring potential was maintained at 1.2 V to obtain RRDE voltammograms used to calculate the hydrogen peroxide yield, $X_{H_2O_2}$. The ORR was measured by $j = j_O - j_N$, the difference between the current per unit geometrical area, S, of the disk electrode obtained in N_2 ($j_N = I_N S^{-1}$) and in O_2 ($j_O = I_O S^{-1}$).

3. Results and discussion

3.1. Catalyst synthesis and crystal structure, morphology

Fig. 1(a) schematically depicts the synthesis of the N, P, S-TiO_2/S-TiN catalysts (see also S1; ESI†) and the roles of dopants and supports. First, N, P-TiO_2 layer catalysts were formed on S-TiN by the pyrolysis of precursor powders prepared from titanium oxysulfate, urea, and hypophosphorous acid using the previously reported solution phase combustion route.[28] The N, P-TiO_2/S-TiN catalysts were then mixed with NH_4F and annealed under N_2 gas. The surface N, P-TiO_2/S-TiN was etched during NH_4F-annealing due to the decomposed HF from NH_4F. Sulfur species inside the bulk TiN appeared on the surface as substitutional dopants for TiO_2. Furthermore, the bulk TiN was oxidized to display hetero-phase junctions with two TiO_2 polymorphs: anatase and rutile.

The effect of the NH_4F-annealing on the bulk crystal structures of the catalysts was evaluated using XRD patterns, as shown in Fig. 1(b). Similar to previous studies on N, P-TiO_2/S-TiN (Fig. S1, ESI†),[27,28] a single TiN phase is observed before NH_4F-annealing. Both anatase and rutile TiO_2 phases appear after the NH_4F-annealing at 1223 K under N_2 gas. The process is as follows: NH_4F decomposes at ~398 K to produce NH_3 and HF gases.[30] Subsequently, part of the TiN reacts with HF to form TiF_3 at elevated temperatures in the range 473–573 K.[31] TiF_3 is not a stable chemical, and the results shown in Fig. 1(b) indicate that it reacts with trace O_2 molecules contaminating the N_2 gas during annealing to form anatase/rutile TiO_2. Indeed, the single TiN phase persists even when the gas flowing during annealing was changed to 10% v/v H_2/Ar (Fig. S3, ESI†). Thus, the N_2 atmosphere is necessary to produce a mixture of anatase/rutile TiO_2 and TiN phases during the annealing with NH_4F. The crystal structure of N, P, S-TiO_2/S-TiN on the top surface is different from the bulk, as shown in Fig. 1(c). As the ORR is a surface reaction, it was evaluated using ultraviolet (UV)-Raman spectroscopy, which is highly sensitive to surfaces.[32] Five clear peaks are observed at ~145, 198, 401, 521, and 636 cm^{-1}, which are assigned to the E_g, E_g, B_{1g}, B_{1g}, and E_g vibration modes of anatase TiO_2, respectively.[32,33] A weak peak at ~441 cm^{-1} is an E_g vibration mode of rutile TiO_2.[33] The absence of peaks from TiN indicates that the surface of TiN was oxidized to form TiO_2 layers. The morphology of these different phases in N, P, S-TiO_2/S-TiN was characterized using TEM. Clear lattice fringes with interplanar distances of 0.35 and 0.25 nm are observed at the inner cores in Fig. 1(d) and S4 (ESI),† which correspond well to the (1 0 1) plane of anatase and rutile TiO_2, respectively. These two phases are directly connected to each other *via* a hetero-phase junction, as indicated by the circle. In addition, the outer surfaces indicated by the dashed lines are disordered to show no clear fringes. Such disordered surfaces are known to promote ORR activity of N, P-TiO_2/S-TiN[28] and N-TiO_2/S-TiN.[34] Other plane combinations of anatase (1 0 1)-rutile (1 1 0) and anatase (1 0 1)-TiN (2 0 0) are displayed in Fig. S4 (ESI),† and these different phases are also directly connected to each other *via* the hetero-phase junction. These results indicate that the bulk of the N, P, S-TiO_2/S-TiN is composed of anatase/rutile TiO_2 and TiN and contains hetero-phase junctions between anatase and rutile or anatase and TiN. On the other hand, the outermost surface consists mostly of TiO_2.

3.2. Chemical states

The oxidized outermost surface is also verified by XPS, as shown in Fig. 1(e). The Ti 2p level splits into Ti $2p_{3/2}$ and $2p_{1/2}$ sublevels to display doublets at three different binding energies. In the Ti $2p_{3/2}$ region, the highest peak at ~459 eV is assigned to Ti-atoms in the TiO_2 lattice while weak shoulders at ~457 and ~455 eV are assigned to those in N-doped TiO_2 and TiN, respectively.[35,36] Thus, the surface is mostly TiO_2 phases, which is consistent with the results of UV-Raman analyses. Four different chemical states are observed from the doped N-atoms. The highest peak at ~401 eV is assigned to interstitial N-atoms in TiO_2, while two peaks at ~399 and ~397 eV are substitutional N-atoms in TiO_2.[37–39] The peak at a low binding energy of ~396 eV is assigned to N-atoms in TiN.[35,36] Therefore, most of the N-atoms on the surface are embedded in the TiO_2 lattice. In the P 2p region, a peak is observed at ~134 eV, which is assigned to cationic pentavalent phosphorous atoms (P^{5+}) which substituted for Ti-atoms in TiO_2.[40] No peaks are observed at ~129 eV, indicating the absence of anionic phosphorous atoms (P^{3-}). These chemical states were also observed in our previous

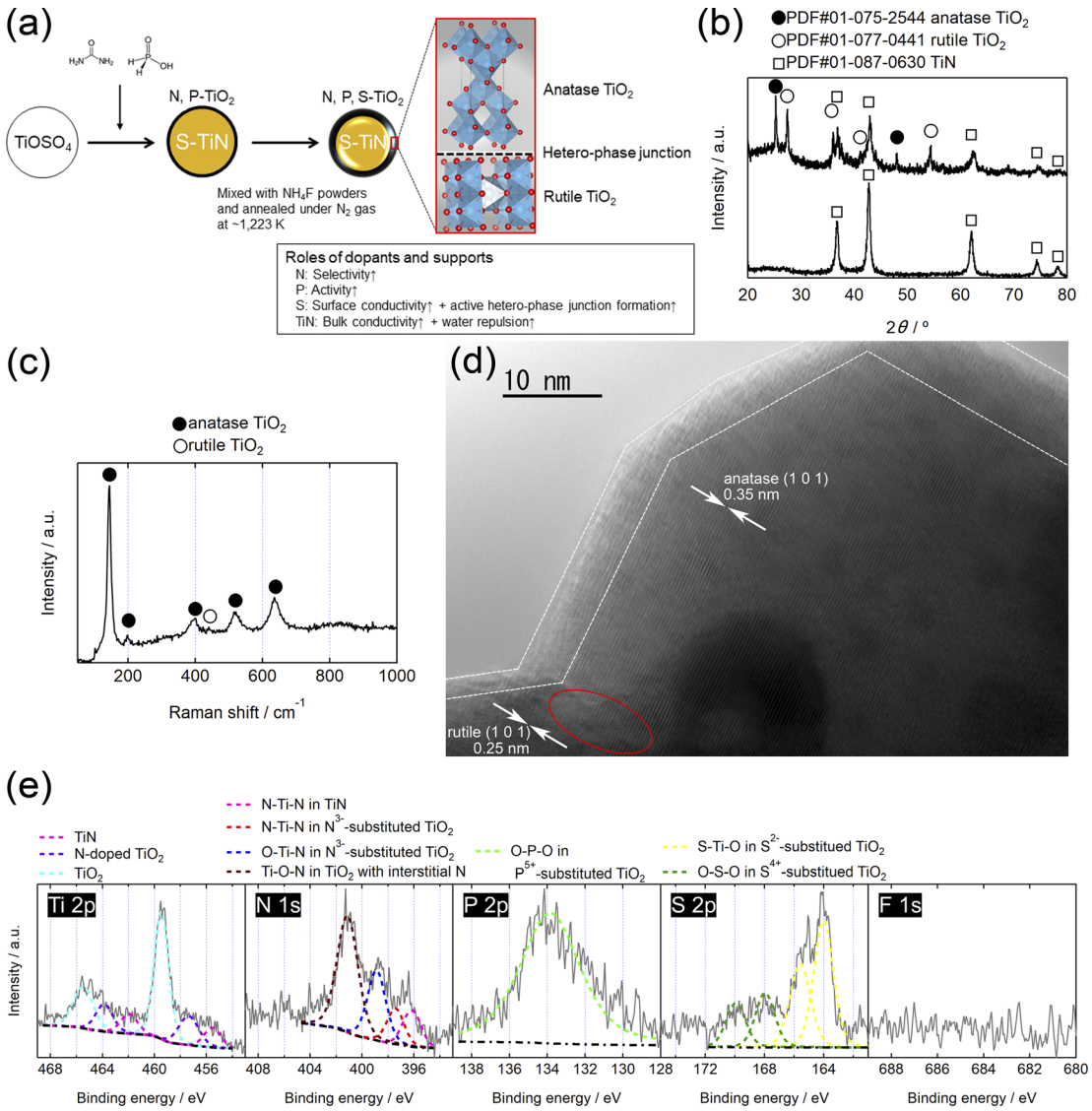

Fig. 1 (a) Schematic diagram for the synthesis of N, P, S-TiO_2/S-TiN and the roles of dopants and S-TiN supports, (b) X-ray diffraction (XRD) patterns of (top) N, P, S-TiO_2/S-TiN after NH_4F-annealing at 1223 K and (bottom) N, P-TiO_2/S-TiN before NH_4F-annealing, (c) Ultraviolet (UV)-Raman spectrum, (d) transmission electron microscopy (TEM) image, and (e) X-ray photoelectron (XP) spectra of N, P, S-TiO_2/S-TiN.

works on N, P-TiO_2/S-TiN without the NH_4F-annealing used in this study (Fig. S2, ESI†),[27,28] although an unexpected difference is observed in the S 2p spectrum. The clear doublets at ~164 and ~166 eV are the S $2p_{3/2}$ and $2p_{1/2}$ peaks, respectively, of divalent anionic sulfur atoms (S^{2-}) substituted for O-atoms in the TiO_2 lattice, while the smaller peaks at ~168 and ~170 eV with higher binding energy are the S $2p_{3/2}$ and $2p_{1/2}$ peaks, respectively, which are tetravalent cationic sulfur atoms (S^{4+}) substituted for Ti-atoms in TiO_2.[41,42] The binding energy of anionic sulfur species doped into TiN is lower than that observed in Fig. 1(e), ~163 eV,[43] ruling out the presence of such species on the surface of N, P, S-TiO_2/S-TiN. Unlike N-doped TiO_2, no clear peak shifts in the Ti 2p regions have been reported for TiO_2 doped with S^{2-} and S^{4+}.[41] In XPS, no peak was detected from the S 2p region in the previous N, P-TiO_2/S-TiN catalysts without NH_4F-annealing (Fig. S2, ESI†)[27,28] or in the current N, P-TiO_2/S-TiN before NH_4F-annealing (Fig. S5, ESI†). However, sulfur species were detected on EDS in the N, P-TiO_2/S-TiN before NH_4F-annealing, with an atomic ratio of sulfur to titanium of 0.075 ± 0.007. These results indicate that sulfur species from titanium oxysulfate precursors are absent on the top surface before NH_4F-annealing but present in the lower layers, since XPS is much more surface sensitive than EDS. As mentioned above, NH_4F should decompose to form NH_3 and HF gases during annealing[30] and the latter product, HF, is a well-known etchant. During annealing, the sulfur-free surface of N, P-TiO_2/S-TiN was etched with HF to expose S-atoms from inside N, P-TiO_2/S-TiN to the surface. Indeed, the TiN content inside N, P-TiO_2/S-TiN was decreased with increasing mass ratio of NH_4F to N, P-TiO_2/S-TiN (Fig. S6, ESI†). The TiN is necessary to give the catalyst conductivity and to improve the ORR activity (Fig. S6, ESI†); however, after NH_4F-annealing, the surface is

an N, P, S-tridoped TiO_2 phase. NH_3, another product of NH_4F-decomposition, further decomposes to N_2 and H_2 at high temperatures, which would be expected to produce a reducing atmosphere, and most of the surface S-atoms are in the reduced state, S^{2-}, rather than the oxidated state, S^{4+}. The EDS analyses on N, P, S-TiO_2/S-TiN revealed that an atomic ratio of fluorine to titanium is at 0.000 ± 0.000. These results and F 1s spectrum shown in Fig. 1(e) indicate that there are no fluorine species in the bulk or surface of N, P, S-TiO_2/S-TiN. Another possible role of the subsurface TiN is to "support" facilitating ORR process. Seifitokaldani *et al.* reported that TiN (2 0 0) facet showed a high activity for both (i) converting OH intermediate to water molecules and (ii) removing the produced water molecules during ORR by using a density functional theory (DFT) calculation.[44] These two steps are necessary for the ORR after the first dissociative adsorption of O_2 molecules which proceeded on the surface N, P, S-TiO_2. Particularly, the step (ii) could proceed faster on TiN (2 0 0) facet than the N, P, S-TiO_2 as TiO_2 is hydrophilic in general. Therefore, TiN could support ORR by both giving the catalyst conductivity and helping the process, particularly by removing the produced water molecules.

3.3. ORR activity and selectivity

The NH_4F-annealing conditions such as temperature, duration, N_2-gas flow rate, and mass ratio of NH_4F to N, P-TiO_2/S-TiN were systematically optimized to maximize the ORR activity (Fig. S6 and S7, ESI†). The RDE voltammograms of the optimized N, P, S-TiO_2/S-TiN and previously reported N, P-TiO_2/S-TiN[28] are shown in Fig. 2(a). The j from N, P, S-TiO_2/S-TiN outperforms N, P-TiO_2/S-TiN at any E. The half-wave potential (*i.e.*, E where half of the maximum j is obtained) has been used to measure the ORR activity of catalysts, and hereafter is denoted as $E_{1/2}$. The $E_{1/2}$ of N, P, S-TiO_2/S-TiN reached 0.72 V, which is 0.08 V higher than that of N, P-TiO_2/S-TiN, and higher than that of any other carbon-support-free, or even carbon-supported, oxide/oxynitride catalysts reported to date, including ZrO_xN_y-MWCNT[24] (Table S1, ESI†). If ORR proceeds *via* a two-electron reaction, hydrogen peroxide is produced (eqn (4)).

$$O_2 + 2H^+ + 2e^- \rightarrow H_2O_2 \quad (4)$$

The produced H_2O_2 molecules decompose membranes and a perfluorosulfonate ionomer in catalyst layers to deteriorate the performance of PEFCs.[45] The H_2O_2 yield measured by RRDE voltammograms, $X_{H_2O_2}$, is plotted as a function of E in Fig. 2(b). Less than half of $X_{H_2O_2}$ is obtained from N, P, S-TiO_2/S-TiN when compared with N, P-TiO_2/S-TiN at $E \geq 0.6$ V, which is an operating potential range for FCVs.[46] Therefore, N, P, S-TiO_2/S-TiN displays higher ORR activity and selectivity toward the four-electron reaction than those of previously reported N, P-TiO_2/S-TiN. The N, P, S-TiO_2/S-TiN was synthesized by annealing N, P-TiO_2/S-TiN and NH_4F under N_2 gas. The NH_4F-annealing produced etchant HF to (1) convert a single TiN phase of N, P-TiO_2 to a mixture of anatase/rutile TiO_2 and TiN phases of N, P, S-TiO_2/S-TiN and (2) expose S-atoms from the inside of N, P-TiO_2/S-TiN to the surface of N, P, S-TiO_2/S-TiN, where they

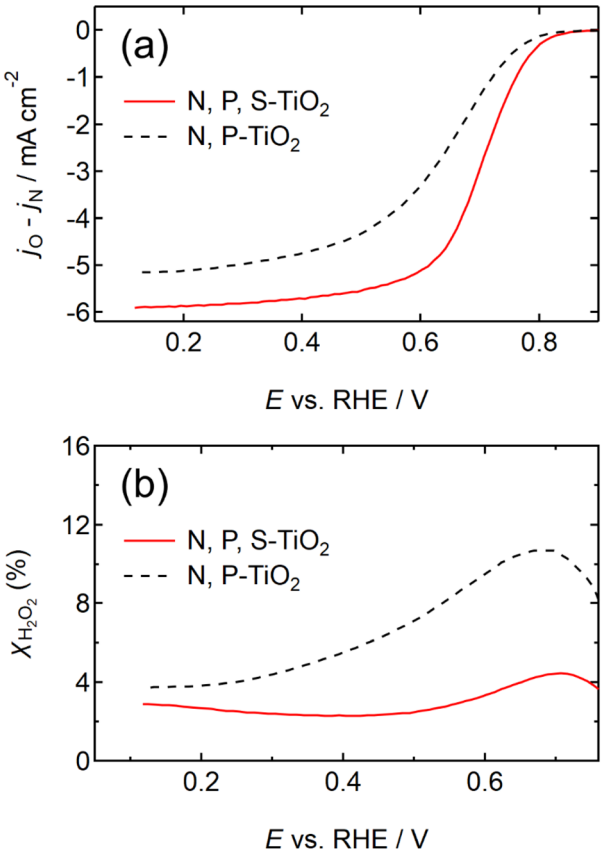

Fig. 2 (a) Rotating disk electrode (RDE) voltammograms and (b) hydrogen peroxide yield *versus* potential ($X_{H_2O_2}$– E) curves of N, P, S-TiO_2/S-TiN catalyst after NH_4F-annealing at 1223 K and N, P-TiO_2/S-TiN catalyst. The N, P-TiO_2/S-TiN catalyst's curves were reproduced with permission.[28] Copyright 2020, American Chemical Society. The scans were performed in N_2 and O_2 atmospheres at a rotation speed of 1500 revolutions per minute (rpm) and a cathodic scan rate of −5 mV s^{-1} in 0.1 mol dm^{-3} H_2SO_4 solution.

mostly substituted for O-atoms in the TiO_2 lattice. In previous reports of carbon-support-free N, P-TiO_2/S-TiN or N-TiO_2/S-TiN synthesized *via* the solution phase combustion route used in this study,[27,28] all XRD patterns displayed a single TiN phase, while the surface was rutile TiO_2 phase according to Raman analyses with a visible laser (Fig. S1, ESI†). When the flowing gas was N_2 during the NH_4F-annealing, anatase/rutile TiO_2 phases appeared in N, P, S-TiO_2/S-TiN due to oxygen contaminants in N_2 flowing in the tube furnace. However, when the flow gas was changed to 10% v/v H_2/Ar instead of N_2 with an identical gas flow rate, the oxygen contaminants were reduced by H_2, leaving a single TiN phase (Fig. S3, ESI†). As a result, much lower activity was observed when the flow gas was 10% v/v H_2/Ar gas than when N_2 was used (Fig. S3, ESI†). These results indicate that a new active site could be formed in the anatase/rutile TiO_2 phases of N, P, S-TiO_2/S-TiN, which is in contrast to previously reported N, P-TiO_2/S-TiN and N-TiO_2/S-TiN catalysts. Anatase/rutile hetero-phase junctions have recently been used to enhance the electrocatalytic activity of TiO_2 for the oxygen evolution reaction (OER)[47] and the selective nitrate reduction to

ammonia.[48] Since the conduction band minimum of rutile is higher than that of anatase, electrons are transferred from rutile to anatase and rutile becomes positively charged.[47,48] The positively charged site acts as a Lewis acid, attracting and dissociating the O-atoms of the O_2 molecule,[49] which is the first step for the ORR. Furthermore, the d-band center of Ti in rutile relative to the Fermi level is upshifted by the electron transfer to anatase. In general, the upshift/downshift of d-band center of transition metals strengthens/weakens the interaction between the metal and intermediates formed during the catalytic reactions.[50–54] When the interaction between reaction intermediates and the catalyst is too strong, the desorption of the intermediates or the next reaction step becomes the rate determining step to delay the overall reaction. On the other hand, too weak interaction also delays the reaction. An optimum adsorption strength of intermediates for various catalytic reactions on several PGM and PGM-free catalysts has been suggested; hydrogen evolution reaction (HER) on P-doped TiO_2 supported Ru cluster catalyst,[50] ORR on various binary/ternary oxide supported Pt catalysts,[51] ORR on activated N-doped porous carbon supported Pt skin shell covered on Pt_3Co bimetallic core catalyst,[52] ORR and OER on Co_3O_4 shell covered on Co core catalyst[53] and ORR on Zn–N–C catalyst.[54] Four-electron (eqn (2)) and two-electron ORR (eqn (4)) in acidic media have been assumed to proceed *via* several elementary steps described by eqn (2a)–(2e) and (4a)–(4c), respectively on conventional catalysts[55,56] and oxynitride catalysts.[57]

Four electron ORR

$$O_2 + * \rightarrow O_2^* \quad (2a)$$

$$O_2^* + H^+ + e^- \rightarrow HO_2^* \quad (2b)$$

$$HO_2^* + H^+ + e^- \rightarrow H_2O + O^* \quad (2c)$$

$$O^* + H^+ + e^- \rightarrow HO^* \quad (2d)$$

$$HO^* + H^+ + e^- \rightarrow H_2O + * \quad (2e)$$

Two electron ORR

$$O_2 + * \rightarrow O_2^* \quad (4a)$$

$$O_2^* + H^+ + e^- \rightarrow HO_2^* \quad (4b)$$

$$HO_2^* + H^+ + e^- \rightarrow H_2O_2 + * \quad (4c)$$

where * is the active site. After the adsorption of O_2 molecules on the positively charged rutile surface of N, P, S-TiO_2/S-TiN, a peroxy intermediate HO_2 is produced in both four electron and two electron ORR processes (eqn (2b) and (4b)). When the interaction between HO_2 and * is too weak or too strong, it inhibits the breaking of O–O bonding in the HO_2 to delay ORR process to favor two electron reactions. Cheng group recently reported that positively charged Zn atoms in their Zn–N–C catalyst facilitate the adsorption of O_2 and reaction intermediates by the upshift of the d-band center of Zn to promote electron transfer and enhance the intrinsic ORR activity in alkaline media.[54] Although the ORR pathway is different between the alkaline media and acidic counterparts used in this study, the HO_2 intermediate is also produced during ORR in alkaline media. Therefore, the mechanism similar to the positively charged Zn atoms in Zn–N–C catalysts reported by Cheng group is expected for positively charged rutile TiO_2. As the rutile at hetero-phase junctions interacts with HO_2 strongly owing to the upshift of d-band center of Ti as electrons are transferred from the rutile to anatase, it could facilitate adsorption of HO_2 to enhance ORR activity and selectivity towards four electron reaction (eqn (2b) and (2c)). In contrast, anatase directly connected to rutile *via* the hetero-phase junction is expected to interact with HO_2 weaker than the rutile as the d-band center of Ti in anatase downshifted owing to the transferred electrons from rutile. If the interaction between rutile and HO_2 is too strong, ORR can proceed on anatase in the vicinity of rutile due to the weaker adsorption strength of anatase than rutile. Therefore, one possible mechanism for the enhancement of ORR activity on N, P, S-TiO_2/S-TiN could be hetero-phase junction formation. Another new product by NH_4F-annealing, substitutional S^{2-} doping into surface TiO_2, could enhance the electrical conductivity of surface TiO_2, which has been used in S^{2-}-doped TiO_2 for sodium ion battery anodes[41] and N^{3-}, S^{2-} codoped TiO_2 for high-rate lithium ion battery anodes.[42] Indeed, N, P-TiO_2/TiN synthesized from sulfur-free titanium source shows higher Tafel slope and lower ORR activity than N, P, S-TiO_2/S-TiN even after the NH_4F-annealing under the conditions identical to those of N, P, S-TiO_2/S-TiN (Fig. S8, ESI†). Another role of sulfur is to inhibit the complete phase transition of anatase to rutile at the high annealing temperature to leave anatase/rutile hetero-phase junctions, which are active toward ORR. Sulfur-doping is known to increase the anatase content in TiO_2 synthesized *via* both a low temperature hydrothermal route[58] and a high temperature annealing route.[59] Similar to these previous reports, anatase content in N, P, S-TiO_2/S-TiN is higher than rutile counterpart even after the high temperature NH_4F-annealing at 1223 K as shown in Fig. 1(b). Therefore, substitutional S^{2-} doping indirectly tuned the strength of ORR intermediates with TiO_2 as mentioned above by forming the anatase/rutile hetero-phase junctions to keep the anatase phase after the NH_4F-annealing. Precise control of the adsorption strength of ORR intermediates by for example, controlling the amount of oxygen vacancy[53] is our next research topic. The grain size of TiO_2 is also reported to be decreased by sulfur-doping to increase the surface area.[58]

Based on the results obtained in this study and previous studies on N, P-TiO_2/S-TiN,[27,28] the roles of three dopants, N, P and S are proposed as follows. Substitutional N^{3-} and P^{5+} dopants have promoted ORR selectivity and activity, respectively of N, P-TiO_2/S-TiN.[28] After NH_4F annealing used in this study, the surface TiO_2 is doped with S^{2-} anions. The S^{2-} substituted for O-atoms in TiO_2 to increase both the surface conductivity and anatase content, which is the origin of the significantly enhanced ORR activity and selectivity towards four electron reaction *via* forming the anatase/rutile hetero-phase junctions. S-doped TiN "supports" both the bulk conductivity[60] and facilitating ORR *via* removing water from the active

sites continuously[44] even after the durability tests, which are shown in the next subsection.

3.4. Durability against fuel cell startup and shutdown protocol

As N, P, S-TiO_2/S-TiN catalysts are free from carbon supports, they are expected to be tolerant to the high potentials faced by FCVs during startup and shutdown. The durability of N, P, S-TiO_2/S-TiN, which showed the highest activity level, was investigated using the common protocol for FCVs proposed by the Fuel Cell Commercialization Conference in Japan (FCCJ) in 2011.[46] The E was cycled between 1.0 and 1.5 V at 0.5 V s^{-1} to simulate the startup/shutdown of FCVs.[46] The RDE voltammograms before and after 5000 cycles are shown in Fig. 3. To compare the startup/shutdown durability of N, P, S-TiO_2/S-TiN catalyst with other limited number of non-PGM catalysts reported to date, the cycle number was selected at 5000 as most works performed below 5000 of startup/shutdown cycles (Table S2, ESI†). Excellent durability within the stringent protocol is observed from N, P, S-TiO_2/S-TiN, showing only a 0.02 V decrease in $E_{1/2}$ after 5000 cycles, which is one-quarter of that shown by N, P-TiO_2/S-TiN under identical conditions (0.08 V).[28] As mentioned in the introduction, carbon oxidation leads to a severe loss of activity in both PtCo/C and PGM-free catalysts. Most studies into PGM-free catalysts investigated durability with a protocol based on <1.0 V (typically between 0.6 and 1.0 V). A limited number of publications have investigated durability to potentials >1.0 V, with a comparison of changes in $E_{1/2}$ during potential cycling provided in Table S2 (ESI†). State-of-the-art Fe/N/C catalysts display significant $E_{1/2}$ losses, and often show no limiting current plateaus. The durability of N, P, S-TiO_2/S-TiN to the startup/shutdown protocol ranks the highest among PGM-free catalysts. While the initial activity of N, P, S-TiO_2/S-TiN ($E_{1/2}$ of 0.72 V) is still lower than that of state-of-the-art M/N/C catalysts,[19,21,22] its durability against startup/shutdown cycles remains the highest. A similar durability was also observed for two other N, P, S-TiO_2/S-TiN catalysts synthesized under different conditions (Fig. S9, ESI†). The extent of titanium ions dissolved from all three N, P, S-TiO_2/S-TiN catalysts in the electrolyte solution after 5000 cycles, as shown in Fig. 3 and S9 (ESI),† was below the detection limit of the inductively coupled plasma (ICP) spectrometer, indicating excellent stability of N, P, S-TiO_2/S-TiN in bulk. The bulk stability suggests the excellent durability of S-TiN supports. Although the surface conductivity of N, P, S-TiO_2/S-TiN is significantly enhanced by S^{2-}-doping into TiO_2 as discussed in the previous subsection, S-TiN supports should be the origin of bulk conductivity as a well-known metallic nitride, TiN displays 17 orders of magnitude higher electrical conductivity than that of the semiconductor TiO_2.[60] The stable activity shown in Fig. 3 and S9† and the ICP analyses on the electrolyte solution after the tests indicate that S-TiN did not dissolve to keep the conductivity during the 5000 startup/shutdown cycles.

The surface stability was next examined by XPS, as shown in Fig. 4. The Ti 2p, N 1s and S^{2-} peaks in the S 2p spectra remained unchanged after 5000 cycles, indicating that these surface chemical states are highly stable. Due to the use of Nafion in the catalyst layer, the stability of S^{4+} cannot be evaluated for the N, P, S-TiO_2/S-TiN catalyst after 5000 cycles because the contribution of the sulfonate group of Nafion and N, P, S-TiO_2/S-TiN cannot be separated. The P 2p spectrum changed to indicate loss of P^{5+} after 5000 cycles. These results suggest that at least the Ti-atoms and anionic dopants which substituted for O-atoms in the TiO_2 lattice are stable. In previous studies on N, P-TiO_2/S-TiN, the Ti 2p, N 1s and P 2p spectra all changed significantly during 5000 cycles from 1.0 to 1.5 V, with the loss of N- and P-atoms from the surface of the TiO_2 lattice.[27,28] Chen *et al.* reported that oxidative annealing of the N-doped TiO_2 in air stabilized N-atoms in the TiO_2 lattice.[61] Although air-annealing reduced the amount of nitrogen in TiO_2, the surviving N-atoms were stable and were not removed during the photocatalytic oxidation of ethylene under highly oxidizing conditions. As a result, the Ti 2p and N 1s spectra of the N-doped TiO_2 did not change significantly during the photocatalytic oxidation of ethylene, and no significant change in photocatalytic performance was observed.[61] In the work of Chen *et al.*,[61] the oxidant that removes the N-atoms from the

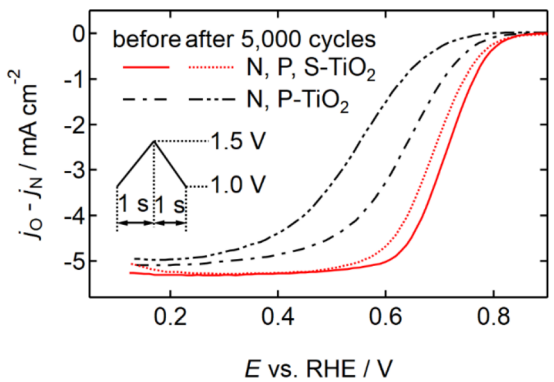

Fig. 3 RDE voltammograms of N, P, S-TiO_2/S-TiN after NH_4F-annealing at 1133 K before (solid curve) and after (dashed curve) 5000 potential cycles between 1.0 and 1.5 V *vs.* reversible hydrogen electrode (RHE) at 0.5 V s^{-1} in 0.1 mol dm^{-3} H_2SO_4 solution. Before and after 5000 cycles, the scans were performed in N_2 and O_2 atmospheres at a rotation speed of 1500 rpm and a cathodic scan rate of −5 mV s^{-1} for evaluating the activity. For reference, RDE voltammograms of N, P-TiO_2/S-TiN before (dash dotted curve) and after (dash double dotted curve) 5000 cycles are also shown with permission.[28] Copyright 2020, American Chemical Society.

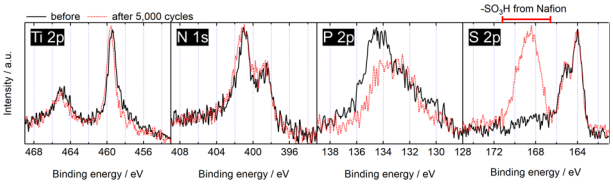

Fig. 4 XP spectra of N, P, S-TiO_2/S-TiN catalyst before (solid curves) and after (dashed curves) 5000 potential cycles between 1.0 and 1.5 V *vs.* RHE at 0.5 V s^{-1} in 0.1 mol dm^{-3} H_2SO_4 solution. The N, P, S-TiO_2/S-TiN catalyst after 5000 cycles contains Nafion ionomer used in the catalyst layer.

TiO_2 lattice without the air-annealing was photogenerated holes ($2N^{3-} + 6h^+ \rightarrow N_2$) produced by visible light irradiation from a 500 W Xe-arc ramp.[62] This differs from the oxidant used in this work; *i.e.*, high potential sites in acidic media. However, one reason for the stabilization of N-atoms in the TiO_2 lattice of N, P, S-TiO_2/S-TiN is that NH_4F-annealing oxidatively forms the TiO_2 phases from TiN, during which N-atoms are embedded in the TiO_2 lattice. The results from Chen *et al.*[61] and this study suggest that to avoid oxidation of the doped TiO_2-based materials during the oxidative catalytic conditions, an oxidative annealing of the material before use will be an effective pathway. Indeed, these phases are sufficiently stable that the XRD patterns remain unchanged after ORR (Fig. S10, ESI†). This is similar to the phase stability of oxynitride photocatalysts during photocatalytic reactions.[62] Furthermore, the morphology of N, P, S-TiO_2/S-TiN did not change significantly during the 5000 cycles (Fig. S11, ESI†) which indicates the structural stability.

4. Conclusions

N, P-TiO_2 layer catalysts formed on S-doped TiN were annealed with NH_4F under N_2 gas to dramatically improve their ORR activity and durability against startup/shutdown cycles for FCVs. NH_4F-annealing oxidized the N, P-TiO_2/S-TiN, resulting in the formation of S-doped TiN-supported N, P, S-tridoped TiO_2 catalysts. The anatase and rutile TiO_2 appeared in the bulk, with the remaining TiN during NH_4F-annealing forming hetero-phase junctions that produced positively charged ORR active sites. The NH_4F-annealing exposed sulfur species from inside the core to the surface, forming anionic S^{2-}-substituted TiO_2 with enhanced ORR activity. The $E_{1/2}$ after NH_4F annealing improved by 0.08 V, reaching 0.72 V, which is higher than that of any other oxide/oxynitride catalyst reported to date. Although the improved $E_{1/2}$ is still lower than that of state-of-the-art M/N/C catalysts, the N, P, S-TiO_2/S-TiN exhibited excellent durability against startup/shutdown cycles. After 5000 cycles at high potential between 1.0 and 1.5 V, the decrease in $E_{1/2}$ was only 0.02 V, which is among the highest durability of any PGM-free catalysts. The anionic dopants and Ti-atoms on the surface are stable, are not removed even after 5000 cycles, and remain active. Simple NH_4F-annealing with the formation of hetero-phase junctions as well as S^{2-} substitution of O-atoms in TiO_2 lattice has been shown to be a new route to improve both ORR activity and startup/shutdown durability and reduce the cost of FCVs. In the proposed mechanism for the enhanced activity and durability, ORR starts from the O_2 adsorption on positively charged rutile TiO_2 followed by smooth adsorption/desorption of reaction intermediates at the hetero-phase junction formed by the S^{2-}-substitution. Validation of the proposed mechanism, precise control of S^{2-} doping level and stabilization of P^{5+}-dopants could further enhance the ORR activity, and these are our next research topics.

Author contributions

Mitsuharu Chisaka: conceptualization, investigation, data curation, formal analyses, writing – original draft, writing – review & editing, funding acquisition. Jubair A. Shamim: investigation, validation, writing – review & editing. Wei-Lun Hsu: validation, writing – review & editing. Hirofumi Daiguji: investigation, validation, writing – review & editing.

Conflicts of interest

There are no conflicts to declare.

Acknowledgements

The authors acknowledge Yusei Tsushima at Hirosaki University, Keishi Yamashita at Horiba Techno Service Co., and Daisuke Nishiya at Public Nuisance & Medical Research Institute for acquiring TEM images–ED spectra, Raman spectra and ICP spectra, respectively. This work was partially supported by a Grant-in-Aid for Scientific Research, Grant Number JP23H01347 from the Ministry of Education, Culture, Sports, Science and Technology (MEXT) in Japan, and a research grant from Takahashi Industrial and Economic Research Foundation in Japan. The XP spectra were acquired at the University of Tokyo with the support by the Advanced Research Infrastructure for Materials and Nanotechnology in Japan (ARIM) of the MEXT, Proposal Number JPMXP1223UT0203.

Notes and references

1 *World Energy Outlook 2022*, International Energy Agency, 2022, p. , p. 146, **https://iea.blob.core.windows.net/assets/830fe099-5530-48f2-a7c1-11f35d510983/WorldEnergyOutlook2022.pdf**, accessed: Feb. 27, 2024.
2 Japan Automobile Manufacturers Association, Inc, *Active Matrix DB*, **https://www.jama.or.jp/statistics/facts/world/index.html**, accessed: Feb. 27, 2024.
3 W. Jia, Z. Jiang, Q. Wang, B. Xu and M. Xiao, *Transp. Policy*, 2023, **135**, 21.
4 O. Gröger, H. A. Gasteiger and J. P. Suchsland, *J. Electrochem. Soc.*, 2015, **162**, A2605.
5 D. A. Cullen, K. C. Neyerlin, R. K. Ahluwalia, R. Mukundan, K. L. More, R. L. Borup, A. Z. Weber, D. J. Myers and A. Kusoglu, *Nat. Energy*, 2021, **6**, 462.
6 T. Nakamichi, *Nikkei Electronics*, 2022, vol. 6, p. 73.
7 A. Kongkanand and M. F. Mathias, *J. Phys. Chem. Lett.*, 2016, **7**, 1127.
8 M. M. Whiston, I. L. Azevedo, S. Litster, K. S. Whitefoot, C. Samaras and J. F. Whitacre, *Proc. Natl. Acad. Sci. U. S. A.*, 2019, **116**, 4899.
9 C. A. Reiser, L. Bregoli, T. W. Patterson, J. S. Yi, J. D. Yang, M. L. Perry and T. D. Jarvi, *Electrochem. Solid-State Lett.*, 2005, **8**, A273.
10 U. Eberle, B. Müller and R. von Helmolt, *Energy Environ. Sci.*, 2012, **5**, 8780.
11 T. Ioroi, Z. Siroma, N. Fujiwara, S. Yamazaki and K. Yasuda, *Electrochem. Commun.*, 2005, **7**, 183.
12 J. Parrondo, T. Han, E. Niangar, C. Wang, N. Dale, K. Adjemian and V. Ramani, *Proc. Natl. Acad. Sci.*, 2014, **111**, 45.

13 I. Jiménez-Morales, F. Haidar, S. Cavaliere, D. Jones and J. Rozière, *ACS Catal.*, 2020, **10**, 10399.
14 M. Chisaka, W. Nagano, B. Delgertsetseg and T. Takeguchi, *Chem. Commun.*, 2021, **57**, 12772.
15 E. Proietti, F. Jaouen, M. Lefèvre, N. Larouche, J. Tian, J. Herranz and J. P. Dodelet, *Nat. Commun.*, 2011, **2**, 416.
16 C. H. Choi, C. Baldizzone, J. P. Grote, A. K. Schuppert, F. Jaouen and K. J. J. Mayrhofer, *Angew Chem. Int. Ed. Engl.*, 2015, **54**, 12753.
17 K. Strickland, E. Miner, Q. Jia, U. Tylus, N. Ramaswamy, W. Liang, M. T. Sougrati, F. Jaouen and S. Mukerjee, *Nat. Commun.*, 2015, **6**, 7343.
18 Y. Shao, J. P. Dodelet, G. Wu and P. Zelenay, *Adv. Mater.*, 2019, **31**, 1807615.
19 X. Zhao, X. Yang, M. Wang, S. Hwang, S. Karakalos, M. Chen, Z. Qiao, L. Wang, B. Liu, Q. Ma, D. A. Cullen, D. Su, H. Yang, H. Y. Zang, Z. Feng and G. Wu, *Appl. Catal., B*, 2020, **279**, 119400.
20 H. Zhang, L. Osmieri, J. H. Park, H. T. Chung, D. A. Cullen, K. C. Neyerlin, D. J. Myers and P. Zelenay, *Nat. Catal.*, 2022, **5**, 455.
21 X. Xie, C. He, B. Li, Y. He, D. A. Cullen, E. C. Wegener, A. J. Kropf, U. Martinez, Y. Cheng, M. H. Engelhard, M. E. Bowden, M. Song, T. Lemmon, X. S. Li, Z. Nie, J. Liu, D. J. Myers, P. Zelenay, G. Wang, G. Wu, V. Ramani and Y. Shao, *Nat. Catal.*, 2020, **3**, 1044.
22 M. Chen, X. Li, F. Yang, B. Li, T. Stracensky, S. Karakalos, S. Mukerjee, Q. Jia, D. Su, G. Wang, G. Wu and H. Xu, *ACS Catal.*, 2020, **10**, 10523.
23 M. Chisaka, in *Electrocatalysts for Low Temperature Fuel Cells: Fundamentals and Recent Trends*, ed. T. Maiyalagan and V. S. Saji, Wiley-VCH, Weinheim, Germany, 2017, ch. 14.
24 M. Chisaka, A. Ishihara, H. Morioka, T. Nagai, S. Yin, Y. Ohgi, K. Matsuzawa, S. Mitsushima and K. Ota, *ACS Omega*, 2017, **2**, 678.
25 M. Chisaka, Y. Ando, Y. Yamamoto and N. Itagaki, *Electrochim. Acta*, 2016, **214**, 165.
26 M. Chisaka, Y. Yamamoto, N. Itagaki and Y. Hattori, *ACS Appl. Energy Mater.*, 2018, **1**, 211.
27 M. Chisaka and H. Morioka, *Catal. Sci. Technol.*, 2019, **9**, 611.
28 M. Chisaka, R. Xiang, S. Maruyama and H. Daiguji, *ACS Appl. Energy Mater.*, 2020, **3**, 9866.
29 M. Chisaka, R. Xiang, S. Maruyama and H. Daiguji, *Energy Fuels*, 2022, **36**, 539.
30 J. S. Sanghera, P. Hart, M. G. Sachon, K. J. Ewing and I. Aggarwal, *J. Am. Ceram. Soc.*, 1990, **73**, 1339.
31 Y. Lee, C. Huffman and S. M. George, *Chem. Mater.*, 2016, **28**, 7657.
32 J. Zhang, M. Li, Z. Feng, J. Chen and C. Li, *J. Phys. Chem. B*, 2006, **110**, 927.
33 U. Balachandran and N. G. Eror, *J. Solid State Chem.*, 1982, **42**, 276.
34 M. Chisaka, *Phys. Chem. Chem. Phys.*, 2018, **20**, 15613.
35 K. S. Robinson and P. M. A. Sherwood, *Surf. Interface Anal.*, 1984, **6**, 261.
36 N. C. Saha and H. G. Tompkins, *J. Appl. Phys.*, 1992, **72**, 3072.
37 C. D. Valentin, G. Pcchioni, A. Selloni, S. Livraghi and E. Giamello, *J. Phys. Chem. B*, 2005, **109**, 11414.
38 J. Wang, W. Zhu, Y. Zhang and S. Liu, *J. Phys. Chem. C*, 2007, **111**, 1010.
39 G. Wang, Z. Jiang, H. Shi, T. Xiao and Z. Yan, *J. Mater. Chem.*, 2010, **20**, 5301.
40 S. P. Madhusudanan, B. Gangaja, A. G. Shyla, A. S. Nair, S. V. Nair and D. Santhanagopalan, *ACS Sustainable Chem. Eng.*, 2017, **5**, 2393.
41 J. Ni, S. Fu, C. Wu, J. Maier, Y. Yu and L. Li, *Adv. Mater.*, 2016, **28**, 2259.
42 W. Jiao, N. Li, L. Wang, F. Li, G. Liu and H. M. Cheng, *Chem. Commun.*, 2013, **49**, 3461.
43 C. Li, J. Shi, L. Zhu, Y. Zhao, J. Lu and L. Xu, *Nano Res.*, 2018, **11**, 4302.
44 A. Seifitokaldani, O. Savadogo and M. Perrier, *Electrochim. Acta*, 2014, **141**, 25.
45 T. Kinumoto, M. Inaba, Y. Nakayama, K. Ogata, R. Umebayashi, A. Tasaka, Y. Iriyama, T. Abe and Z. Ogumi, *J. Power Sources*, 2006, **158**, 1222.
46 A. Ohma, K. Shinohara, A. Iiyama, T. Yoshida and A. Daimaru, *ECS Trans.*, 2011, **41**, 775.
47 Y. Hu, T. Ding, K. Zhang, B. Li, B. Zhu and K. Tang, *ChemNanoMat*, 2018, **4**, 1133.
48 Z. Wei, X. Niu, H. Yin, S. Yu and J. Li, *Appl. Catal., A*, 2022, **636**, 118596.
49 C. Jia, G. Zhang, W. Zhong and J. Jiang, *ACS Appl. Mater. Interfaces*, 2016, **8**, 10315.
50 S. Zhou, H. Jang, Q. Qin, L. Hou, M. G. Kim, S. Liu, X. Liu and J. Cho, *Angew. Chem., Int. Ed.*, 2022, **61**, e202212196.
51 F. Ando, T. Gunji, T. Tanabe, I. Fukano, H. D. Abruña, J. Wu, T. Ohsaka and F. Matsumoto, *ACS Catal.*, 2021, **11**, 9317.
52 Z. Wang, S. Chen, W. Wu, R. Chen, Y. Zhu, H. Jiang, L. Yu and N. Cheng, *Adv. Mater.*, 2023, **35**, 2301310.
53 W. Wu, R. Chen, S. Chen, Z. Wang and N. Cheng, *Small*, 2023, **19**, 2300621.
54 Y. Tan, Z. Zhang, S. Chen, W. Wu, L. Yu, R. Chen, F. Guo, Z. Wang and N. Cheng, *Adv. Funct. Mater.*, 2024, **34**, 2311337.
55 J. K. Nørskov, J. Rossmeisl, A. Logadottir, L. Lindqvist, J. R. Kitchin, T. Bligaard and H. Jónsson, *J. Phys. Chem. B*, 2004, **108**, 17886.
56 S. Siahrostami, S. J. Villegas, A. H. B. Mostaghimi, S. Back, A. B. Farimani, H. Wang, K. A. Persson and J. Montoya, *ACS Catal.*, 2020, **10**, 7495.
57 M. Chisaka, T. Abe, R. Xiang, S. Maruyama and H. Daiguji, *Phys. Chem. Chem. Phys.*, 2022, **24**, 29328.
58 H. Tian, J. Ma, K. Li and J. Li, *Ceram. Int.*, 2009, **35**, 1289.
59 N. Sharotri and D. Sud, *New J. Chem.*, 2015, **39**, 2217.
60 F. Cardarelli, in *Materials Handbook: A Concise Desktop Reference*, ed. F. Cardarelli, Springer-Verlag, London, UK, 2nd edn, 2008, ch. 10.
61 X. Chen, X. Wang, Y. Hou, J. Huang, L. Wu and X. Fu, *J. Catal.*, 2008, **255**, 59.
62 K. Maeda and K. Domen, *J. Phys. Chem. C*, 2007, **111**, 7851.